Investigating the Structure of Neutron Rich Calcium Isotopes

By

Jacob Hollett

A Thesis Submitted to

Saint Mary's University, Halifax, Nova Scotia

In Partial Fulfillment of the Requirements for the Degree of

Bachelor of Science with Honours in Astrophysics

April, 2021, Halifax, Nova Scotia

Copyright © Jacob Hollett

Approved: Dr. Rituparna Kanungo

Approved: Dr. Greg Christian

Date: April 30, 2021

Investigating the Structure of Neutron Rich Calcium Isotopes

By

Jacob Hollett

Abstract

The behavior of neutron and proton rich nuclei that lie far from the region of stability is a matter of great scientific interest. This is because not only do these nuclei play important roles in stellar nucleosynthesis events such as the r-process, but they also allow us to observe changes in the nuclear shell structure, which helps shape our understanding of the nuclear interaction. This behavior is often attributable to the existence of shell closures, that occur at a few specific numbers of protons and neutrons. Forming a complete understanding of such shell closures requires knowledge regarding the orbital occupancies of these nuclei. Through an experiment conducted at TRIUMF, Canada's particle accelerator center, the orbital occupancies of neutron rich Calcium isotopes have been probed. These nuclei, with a conventional closed proton shell of $Z = 20$, draw interest with new neutron shells signaled at $N=32$ and 34. An overview of the experimental process and subsequent analysis will be detailed throughout the following discussion. The overview of the experiment will detail the conditions and methods used, while the discussion of the analysis will review the steps undertaken towards the construction of ^{50}Ca(d,d)^{50}Ca Q-Value spectra.

Date: April 30, 2021

Table of Contents

List of Figures

Chapter 1
Introduction

1.1   Nuclei both Familiar and Exotic

From the basic building blocks that are protons, neutrons and electrons, the universe assembles the myriad elements we observe on earth and in far off stars and dust. These elements span the incredible range from the most abundant hydrogen, that fuels stars such as our sun, to rare and exotic species such as the heavy actinides, and everything in between. From the oxygen we breathe to the calcium in our bones, everything is composed of nuclei, which consist of protons and neutrons, and the electrons orbiting around them.

Primarily, the elements lighter than iron are formed during nuclear fusion processes that are continuously working away within stars. Elements heavier than iron, however, are thought to be by and large synthesized during catastrophic events such as supernovae and neutron star mergers. Both of these events proceed through a series of proton or neutron captures, and subsequent beta decays, illuminating the vast number of possible combinations of protons and neutrons. Of this vast number we normally

encounter only the groups of stable and long-lived species, but through the production of rare nuclei here on earth, we continually push further towards observing ever more extraordinary systems with their increasingly extreme proton – neutron combinations.

This incredible number of nuclei may be categorized according to their number of protons (Z), their number of neutrons (N), or their sum of protons and neutrons, known as the mass number (A). Nuclei which share the same number of protons but have differing numbers of neutrons are known as isotopes, while nuclei that share the same number of neutrons but differ in number of protons are known as isotones, and finally nuclei which share a mass number are known as isobars.

While the synthesis of elements up to iron in stars through nuclear fusion is currently well understood, the mechanism at play in the violent events previously discussed that account for many of the heavier elements is still not quite in clear focus. This mechanism is known as the rapid neutron capture process, in which nuclei rapidly capture neutrons and successively beta decay, trending towards heavy, stable elements. This process is understood to proceed through rare, short-lived neutron rich nuclei, in which the current theoretical understanding of the nuclear interaction falter. Therein lies the goal of this thesis, to contribute experimental information to aid in the

theoretical modeling of the properties of exotic nuclei, which will in turn help elucidate the rapid neutron capture process.

1.2 The Nuclear Shell Model

Just as electrons arrange themselves into shells as they orbit around the nucleus, so to do the protons and neutrons within it. These nucleons reside in a mean potential resulting mainly from the strong nuclear interaction between them and their immediate neighbors, meaning that a nucleon well inside the nucleus experiences the same interaction regardless of its location. This results in a potential well with a flat bottom and gradually sloping walls. While this potential may not be expressed in exact form, it may be approximated with a simple harmonic oscillator potential. Protons and neutrons independently fill orbitals that are the eigenstates of this potential well according to the Pauli exclusion principle, with energies specified by the principle quantum number (N) and the orbital angular momentum (l). [1]

In order to reconcile experimental results with this model, M.G. Mayer and J.H.D. Jensen added a term to this model describing the coupling between the angular momentum and spin (s) of the nucleons [2][3]. This term results

in a splitting of the harmonic oscillator levels, with the orbital having total

angular momentum (j)

$$j_< = l + \frac{1}{2} \tag{1.1}$$

Becoming lower in energy than the orbital with total angular momentum

$$j_> = l - \frac{1}{2} \tag{1.2}$$

From these arguments of an approximate nuclear potential and spin –

orbit splitting, we come to the formation of nuclear shells, as is depicted in

(Fig 1.1.). Energy gaps between shells identify shell closures, with the number

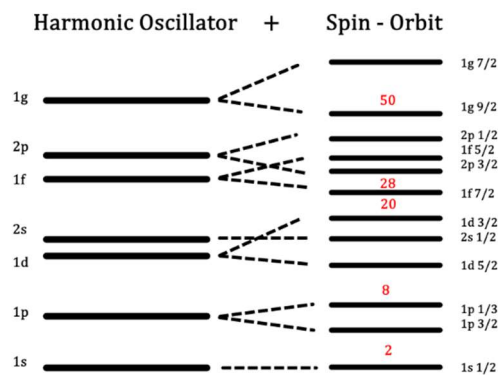of protons or neutrons below a particular gap being referred to as a magic

number.

Figure 1.1: Single particle energies for the harmonic oscillator potential and added spin orbit interaction, with levels labeled N l j, and magic numbers denoted in red.

This shell structure model and the magic numbers arising from it have

proven very successful in the description of both magic and non-magic nuclei,

with the robust properties of magic nuclei such as their high first excited state energies and spherical shapes serving as experimentally observable verification of the model. This well understood description begins to fail however, in exotic nuclei with asymmetric ratios of protons and neutrons such as the neutron rich isotopes the r-process is understood to proceed through. To better understand the changes in shell structure that arise, experimental data regarding these exotic nuclei are needed to guide the improving theoretical descriptions.

1.3 The Evolution of Shell Structure

With the image of a closed shell nucleus such as ^{40}Ca, with its twenty protons and twenty neutrons acting as an inert core, the central mechanism and effect of shell evolution may be illustrated. Any additional nucleons added to the valence orbitals above the inert core serve to influence the energies of the other orbitals above the inert core. This shift is mediated by a component of the nuclear force, and its strength is dependent upon the number of nucleons in the valence orbitals. If the effect proves sufficiently extreme, it

may give rise to new shell closures or efface traditional ones [1]. The effect is
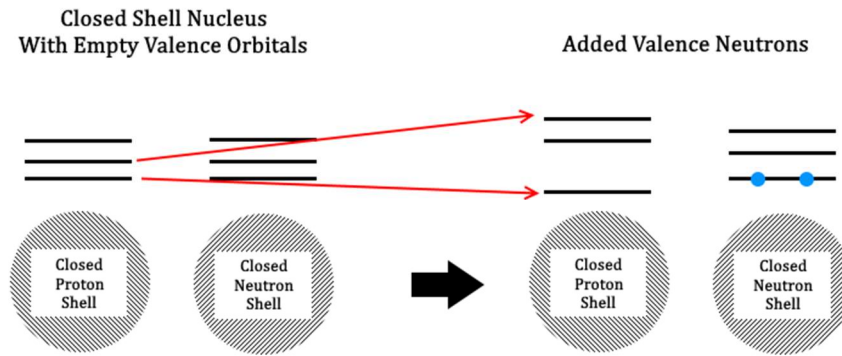
illustrated in (Fig 1.2).

Figure 1.2: Schematic depiction of a closed shell nucleus, and a
nucleus with additional valence neutrons, respectively. The additional
valence neutrons serve to shift the single particle energies of other orbitals.

The effect of shell evolution on magic numbers has been known for

some time, with experimental evidence for the appearance of a new shell gap

$N = 32$ arising in ^{52}Ca being found by A. Huck et. al. in 1985 [4]. In order to

better understand the effects of shell evolution and its driving mechanism,

ever more experimental information is needed on exotic nuclei, to guide

theoretical models in areas such as those where new shell gaps arise, such as

the neutron rich Calcium isotopes.

1.4   New Shell Closures in Neutron-Rich Isotopes

Neutron rich Ca isotopes and nearby species such as Ti [5] have proved themselves to be an excellent testing ground for the effects of nuclear shell evolution and the calculations working to model them, with Ca isotopes being of particular interest due to their traditional closed proton shell of $Z = 20$. A number of studies have focused their attention on the emerging shell gaps understood to be present within the region.

The work discussed in the previous section offered evidence of a new shell gap at $N = 32$ in ^{52}Ca, in the form of the first 2^+ excited state energy, which is often the first excited state in nuclei with even numbers of protons and neutrons. However, it is important to note that while the value reported is strong evidence, and is cited as being well in line with theoretical models, this first 2^+ excited state energy is not a decisive indicator of a shell closure, as it may be affected by a variety of other factors. There may also be uncertainty involved in the spin and parity ($^\pi$) assignment of the observed state, as was the case in the discussed work.

More evidence for an N = 32 shell closure came from measurements of the first 2^+ excited energies of a number of Cr isotopes. A number of studies such as Ref. [6] by R. Chapman, S. Hinds and A.E. Macgregor have reported the first excited state energies of a number of Cr isotopes including ^{52}Cr, ^{54}Cr and ^{56}Cr, with a traditional closed neutron shell of N = 28, N = 30 and N = 32, respectively. While an increase in the first excitation energy of ^{56}Cr was noted as in ^{52}Ca, the question remained whether this excitation energy peaked in the N = 32 isotones or continued to increase as ever more neutrons are added. J.I Prisciandaro et. al. reported the energy of the excited state for ^{58}Cr, which contains thirty four neutrons, finding that it does decrease compared to its N – 2 neighbour [7].

Furthermore, a shell closure at N = 34 had been proposed quite some time ago [8], and became a topic of interest as more exotic nuclei around N = 34 could be more readily produced in facilities worldwide. Ref. [9] by M. Rejmund et. al., proposed to study this possible shell gap through observations of excited states of ^{50,51,52}Ca. In these excited states, a single neutron populates the orbitals $2p_{1/2}$, which is filled in the case of ^{54}Ca, and $1f_{5/2}$. The difference in energy of these orbitals was then inferred, and no evidence for this shell closure was found. A number of other studies focused on observing the first 2^+ excited state in Ti and Cr isotopes, also found no evidence of the shell

closures existence, such as Ref. [5]. Conversely, a later study by D. Steppenbeck et. al., found evidence for its existence in the form of the first 2^+ excited state of ^{54}Ca, reported to be similar to that of ^{52}Ca found more than twenty five years prior [10].

More evidence of both of these shell gaps come in the form of mass measurements of a number of Ca isotopes of mass 51, 52 [11], 53, 54 [12], and 55, 56 and 57 [13]. From these mass measurements, the binding energy of the nuclei, which is the result of all the reactions between the constituent nucleons, may be derived. Further, the two neutrons separation energy, which is defined as the binding energy of a nucleus, subtract the binding energy of a nucleus with two fewer neutrons, may be defined. Through the three mentioned studies, trends in the two neutron separation energy of these nuclei as a function of neutron number are seen to mimic the trends seen in the traditionally magic calcium nuclei, and the nuclei that surround them. For instance, the two neutron separation energy is seen to sharply decrease in nuclei after the traditional magic nucleus ^{48}Ca, as well as ^{52}Ca and ^{54}Ca, as observed in the aforementioned studies.

Evidently, ever more experimental input on the properties of exotic isotopes around these discussed shell gaps is needed to further clarify our understanding of nuclear shell evolution and its effects on exotic isotopes.

Perhaps there is no better case study for this than the Ca isotopic chain, which would benefit from more well defined spin and parity assignments.

1.5 Nuclear Reactions

The majority of the experiments discussed in the previous section went about studying their topic of interest by way of nuclear reactions between a beam of projectile nuclei and stationary target-like nuclei. With exotic nuclei, such as the neutron rich isotopes of interest to this experiment having very short lifetimes, using them to construct a stationary target would be impracticable, as the target would continuously decay. Instead, these exotic nuclei come in the form of a beam, produced in fragmentation reactions between high energy protons and heavy targets.

The result of the reaction between the heavy beam (A) and the light target (b) may come in a number of forms, depending on the reaction that occurs. Regardless of the type of reaction, it is often written in the notation *A(b, d)C*, with the reaction heavy product being denoted (C), and the light product being denoted (d). Generally,

$$A + b \rightarrow C + d \tag{1.3}$$

The first type of reaction that is of interest is scattering, which comes in both elastic and inelastic flavours. In both cases, the participating nuclei remain the same species they were before the reaction.

$$A + b \rightarrow A + b \tag{1.4}$$

However, whereas kinetic energy is also conserved in an elastic reaction, in an inelastic scattering reaction, one or both participants are jolted into an excited state.

$$A + b \rightarrow A* + b* \tag{1.5}$$

The second type of reaction that is of interest is transfer reactions, wherein one or more nucleons are transferred between the participating nuclei during the reaction, which may be represented by the general form (1.3).

The participant species in the experiment detailed by this work were a beam of the isotope ^{50}Ca, and a solid target composed of deuterons. As described above, the result of a reaction between ^{50}Ca and deuterons may come in a variety of forms, such as ^{50}Ca(d,p)^{51}Ca if a neutron is transferred to ^{50}Ca from the deuteron, or ^{50}Ca(d,d)^{50}Ca if the participants scatter, which will be further explored throughout the analysis section.

Chapter 2
Experimental Overview

2.1 Exotic Nuclei Generation

The properties of increasingly short lived and neutron-proton asymmetric nuclei are being probed at particle accelerator facilities across the globe. The topic of discussion for this thesis is the analysis of an experiment that was undertaken at TRIUMF, Canada's particle accelerator center located in Vancouver, British Columbia.

The rare isotope of interest in the experiment, ^{50}Ca, was produced via fragmentation of a Tantalum target by a beam of protons accelerated to 500 MeV by the TRIUMF cyclotron, the worlds largest. These fragmentation and fission reactions in the target produce a wide number of nuclei, not only the species of interest. It is then necessary to separate the isotopes in the beam, and remove unwanted contaminants. This is done by discriminating based on the mass-to-charge ratio of the nuclei of interest. However, this cannot account for all contaminants, resulting in species with similar mass-to-charge ratios of the species of interest, or neighbouring mass 50 isobars that may not

be resolvable from ^{50}Ca remaining in the beam. After the beam is separated, it is next re-accelerated to approximately 7.5 AMeV and delivered to the ISAC charged particle reaction spectroscopy station (IRIS), to undergo the experimental procedure.

2.2 The IRIS Facility

Located in the TRIUMF Isotope Separator and Accelerator (ISAC-II) facility, the IRIS facility is designed to study the elastic and inelastic scattering reactions, as well as the particle transfer reactions that take place between rare isotopes and a stable nucleus as a reaction target. IRIS has a unique target compared to those commonly used, being composed of solid deuterium. Before a beam encounters the target however, it first passes through the Ionization Chamber (IC), a form of proportional counter. After reacting in the target, the product particles make their way into one of a number of charged particle detectors, which are composed of silicon, except for a single cesium iodide scintillator. These components are depicted in Figure 2.1.
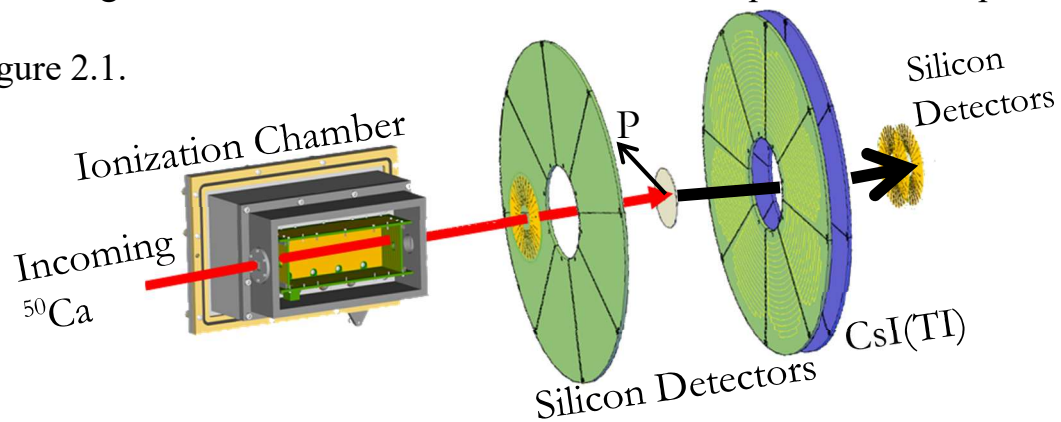
Figure 2.1: Schematic view of IRIS

2.3 The Ionization Chamber

The first apparatus that an incoming rare isotope interacts with in the IRIS set up is the ionization chamber. The IC is a form of gas detector filled with isobutane and kept at a constant pressure of 19.5 Torr. After the incoming beam passes through the chamber's first 30 nm silicon nitride window, it travels through the gas volume of 229 mm, wherein each particle deposits an amount of its energy proportional to the square of its atomic number, and inversely proportional to the particle's kinetic energy, per unit distance. This is expressed in equation 2.1.

$$-\frac{dE}{dx} \propto \frac{Z^2}{E_k} \qquad (2.1)$$

This deposited energy serves to ionize the gas molecules, which drift, under the influence of an electric field produced by the chambers field cage, towards the anode pads. The collected charge is then sent as a voltage signal to the IRIS data acquisition system after being processed through electronic units. The beam of rare isotopes then proceeds through the chambers second

50nm silicon nitride window and into the main chamber scattering chamber, where it encounters the IRIS solid deuterium target.

2.4 The Solid Deuterium Target

After passing through the ionization chamber, the rare isotope beam encounters the IRIS target, with which it participates in a number of different interactions. The target apparatus consists of a thin silver foil, the width of which is on the order of ~ 4 μm. This foil is mounted upon a copper cold cell, cooling the foil to approximately 4 K. A diffuser flows deuterium gas onto this foil, freezing it, and creating typical target thicknesses on the order of $\sim$ 50 μm or $\sim$ 100 μm. This diffuser sits upon an actuator, allowing it to be moved into position to flow deuterium, and back safely out of the beam path, as is shown in Figure 2.3.

The orientation of the target apparatus for this experiment was such that the silver foil faced up stream, meaning incoming beam first encountered the deuterium target, then any resultant particles that scattered forward would first need to pass through the thin silver foil, before passing through a hole at the center of the copper cold cell and finally reaching one of the detectors in the

array. This introduces energy loss in forward scattered particles as they travel through the silver foil.

The greatest benefit of the solid deuterium target come from its density, which aids in maximizing the rate of interactions between it and the rare isotopes of interest, which have characteristically low rates, due to the immense difficulty of their production.

Figure 2.3: Photo of IRIS target apparatus

2.5 The Detector Array

After interacting with the solid deuterium target, the last action of an incoming nuclei at IRIS is coming to rest in one of the several detectors in the array. Upstream of the target apparatus are situated two silicon detectors, an S3 detector and a segmented YY1 detector. Downstream, another YY1 detector is positioned in front of a cesium iodide scintillator, and downstream of these are positioned two more S3 detectors, as is pictured in Fig. 2.1.

The S3 detectors are double sided, silicon detectors segmented into 24 rings on one face, and 32 sections on the opposite face, as is pictured in Figure 2.4. These segmented silicon modules are each kept at a constant operating voltage, which record the energy of any incident particle and allow for the angle of the deposited particle to be distinguished. The upstream S3 detector covers an approximate angular window in the laboratory frame, of 22°, $\Theta_{lab} = 146°$ - 168°. The downstream pair of S3 detectors cover a smaller angular window of approximately $\Theta_{lab} = 2°$ - 7°.

The YY1 are segmented silicon detectors consisting of eight seperate sectors, each with 16 angular segments (Fig. 2.4), which operates in much the same way as the S3 detectors. Once again, this allows for the angle of a

deposited particle to be resolved. Larger than the S3 detectors, the upstream YY1 covers an angular window of approximately $\Theta_{lab} = 122° - 149°$, whereas the downstream YY1 array covers an approximate angular window of $\Theta_{lab} = 29° - 55°$

The cesium Iodide scintillator positioned behind the downstream YY1 is comprised of 16 sections, which have no angular segmentation. However, therein lies the reasoning for its positioning, as while the downstream YY1 detector is angularly segmented, it is not capable of stopping the higher energy light particles such as protons and deuterons that are scattered forward. Together however, any higher energy light particle incident upon both the YY1 and the CsI(TI) detectors may have their incoming angle and a proportion of their energy recorded by the YY1 as it passes through, and may then have their remaining energy recorded by the CsI(TI) as they implant themselves. This configuration allows for scattered light particles to be identified, as protons, deuterons, tritons and alpha particles will all deposit different, distinguishable proportions of their energy between the YY1 and CsI(TI).

Together, the detector array allows for the resultant light and heavy particles of interactions such as $^{50}Ca(d,d)^{50}Ca$ and $^{50}Ca(d,p)^{51}Ca$ to all be

a)   detected, whether they are   b)   scattered forward ($\Theta_{lab} < 90°$)

or backward ($\Theta_{lab} > 90°$) and have their total energy and incident angle recorded, which are vital in the experimental analysis from the beginning of detector calibration to the resulting Q-Value spectrum.
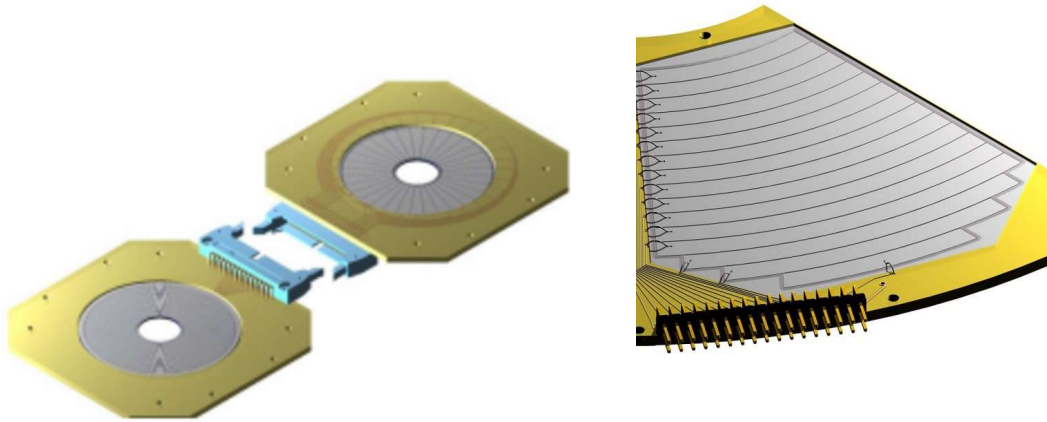

Figure 2.4: a) Image of S3 detector, with both ringed and segmented faces visible. b) One of eight YY1 sectors.

Chapter 3
Experiment Analysis

Turning now to the analysis of the experimental data, a number of steps must be undertaken before any meaningful result may be derived. First, the experimental parameters must be understood, such as the contents of the incoming beam and its energy, as well as the thicknesses of the deuterium target and silver foil. To determine these, the array of detectors must also be calibrated. Only once all of this is complete, may specific interactions between the beam and target be studied.

3.1 Identifying Beam Species

As previously described, when a beam is produced at TRIUMF, it contains a myriad of species, which are then separated based on their mass-to-charge ratio. Meaning, that when the beam arrives at IRIS, it is still not a pure beam of the species of interest, ^{50}Ca, but may contain a number of different nuclei with similar mass-to-charge ratios. These incoming isotopes must then be identified using the ionization chamber. As discussed in section

2.5, the energy deposited by an isotope as it travels through the ionization chamber is proportional to the isotopes Z^2 and inversely proportional to its kinetic energy, meaning that each incoming species of different Z is distinguishable. As an incoming particle passes through the IC and ultimately makes its way into a detector, gates may be made on IC output to select only those events in other detectors that correspond to the gated species, as illustrated in Fig. 3.1.
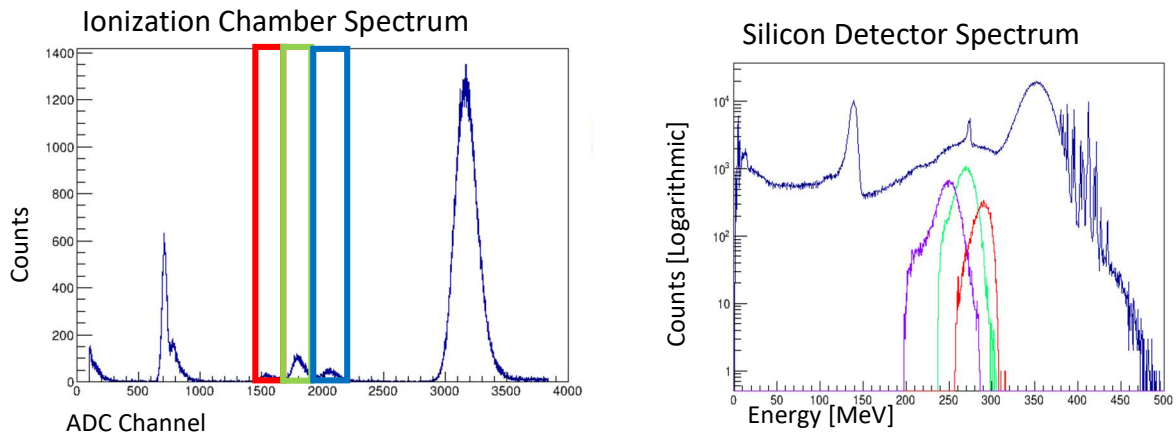

Figure 3.1: Ionization chamber spectra showing beam contents from left to right ^{25}Mg, ^{50}Ca, ^{50}Ti, ^{50}Cr and ^{75}As respectively. Silicon detector spectra with corresponding species identified with IC conditions.

3.2 Detector Calibration

The raw analog voltage signal output by an IRIS detector is digitized and recorded according to its amplitude. This is recorded as an ADC (Analog

to Digital Converter) channel number, which is related to the physical value of the energy deposited in the detector by an incident particle in the following manner.

$$E = g \times (c - p) \hspace{3cm} (3.1)$$

Where E is the energy deposited by the incident particle, g is the gain value, a ratio between deposited energy and output channel number that may not be completely linear across the entire energy regime, and also is in general not the same for different segments of the same detector. It is because of this potential non-linearity that the source chosen to calibrate the detector must be of similar in energy to the particle that will be detected in the experiment, this will be further discussed in a later section. The quantity c is the output channel number, and p is the pedestal value of the detector segment, or the channel number corresponding to zero deposited energy, which is universally not channel zero. In general, the task of calibrating a detector then lies in determining the necessary parameters, the gain and pedestal values, of each detector segment.

3.3 YY1 and Upstream S3 Detectors

The particles detected by the upstream YY1 and S3 detectors covering laboratory angular windows greater than 90° consist of light particles such as the resultant protons in the ^{50}Ca(d,p)^{51}Ca, with the heavier, more energetic beam like particles being restricted to very low angles. With this in mind, the process of calibrating the upstream detectors begins with determining the pedestal, p, of each detector segment. This is done by letting the detectors run idle, with no source of radiation to be detected. The ADC channel at which ambient detector noise is visible is taken to be the pedestal. To determine the gain, a triple alpha source of known energies is observed, and the resultant spectra in each detector segment is fit with three gaussians. The mean of these gaussians, which is in ADC channel number, may then be plotted against the known energies of the triple alpha source, with the slopes of linear fits determining the gain value for each segment. The results of this process may be visualized in Fig. 3.2, with the effect of different sectors having different pedestals visible as the waving nature of the uncalibrated spectrum, and the effect of scaling being visible as the difference in the y-axes.
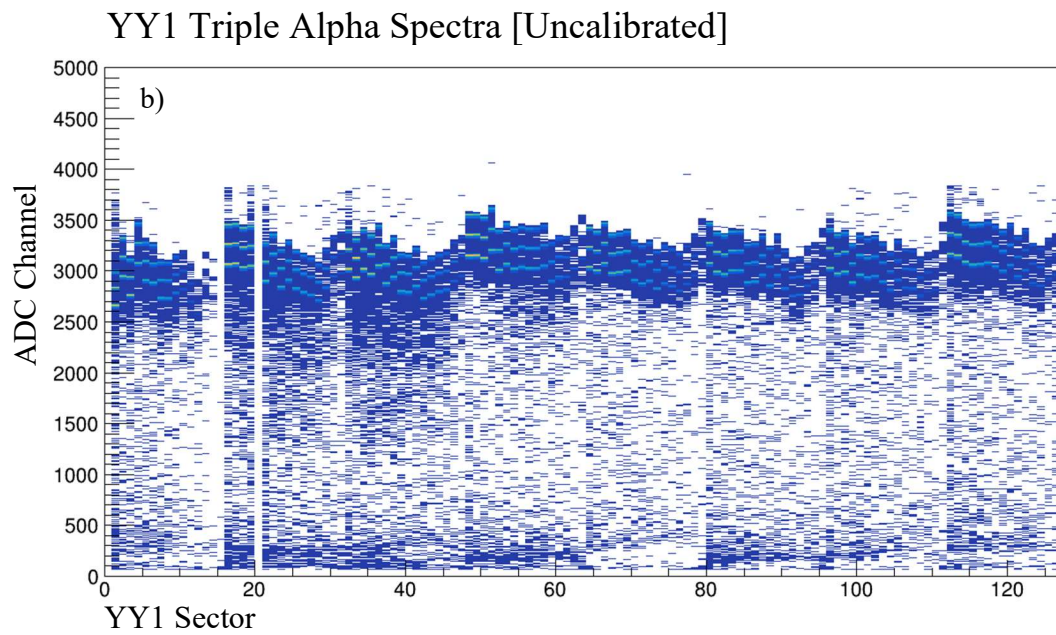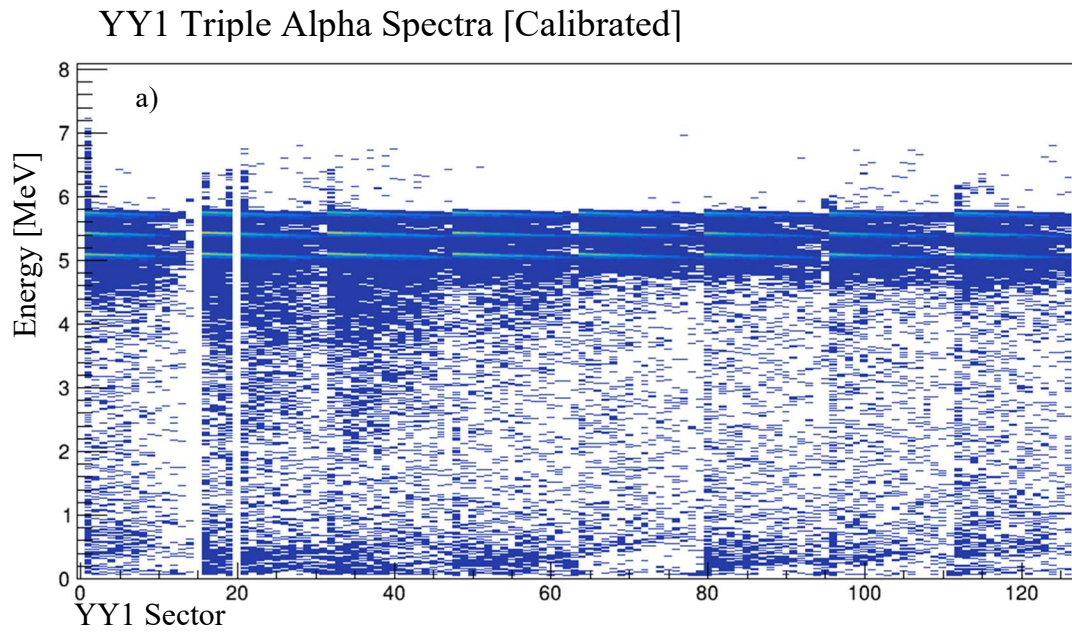
YY1 Triple Alpha Spectra [Calibrated]

a)

YY1 Triple Alpha Spectra [Uncalibrated]

b)

Figure 3.2: Triple alpha source spectra showing all segments of the upstream YY1.

3.4 Silver Foil Thickness Determination

A short time prior to the experiment, the silver foil component of the IRIS target apparatus was replaced. To be able to accurately calibrate further detectors, it is imperative to measure the thickness of this foil, as it is necessary to be able to calculate the energy lost by a particle passing through it. To this end, the triple alpha source previously discussed was again employed. This source consisted of ^{239}Pu, ^{241}Am and ^{244}Cm which emit alpha particles at 5.80 MeV, 5.15 MeV and 5.48 MeV respectively. Spectra were recorded with the previously calibrated detectors, first with the source in front of the foil relative to the detectors, and then behind.

These two spectra are then compared, and an energy difference, as shown in Fig. 3.4, may be observed, after once more fitting each peak with a gaussian and observing the mean. This difference corresponds to the energy lost in the foil by the alpha particle passing through, which as we have previously discussed is proportional to the Z^2 of the particle, and inversely proportional to the particle's kinetic energy, per unit distance traveled through the material. If a particle were to travel through both the silver foil and deuterium target as shown in figure 3.3, the resulting energy may be expressed as

$$E_2 = E_1 - \int_0^{x_1} \frac{dE}{dx_1} dx_1 - \int_0^{x_2} \frac{dE}{dx_2} dx_2 \qquad (3.2)$$

With x_1, x_2 representing the thickness of the target and the foil respectively, and the value of the integrand, the energy lost per unit material, being adopted from well understood stopping power tabulations, an example of which is shown in Fig. 3.5. With only the foil being present in this step, the first integral is zero, and the above steps and tools outlined may be applied, and the foil thickness, which was found to be 4.3 ± 0.3 µm, may be measured. The quoted uncertainty accounts for uncertainties in the recorded means of the fitted gaussians and discrepancies between the values measured for each alpha source species.
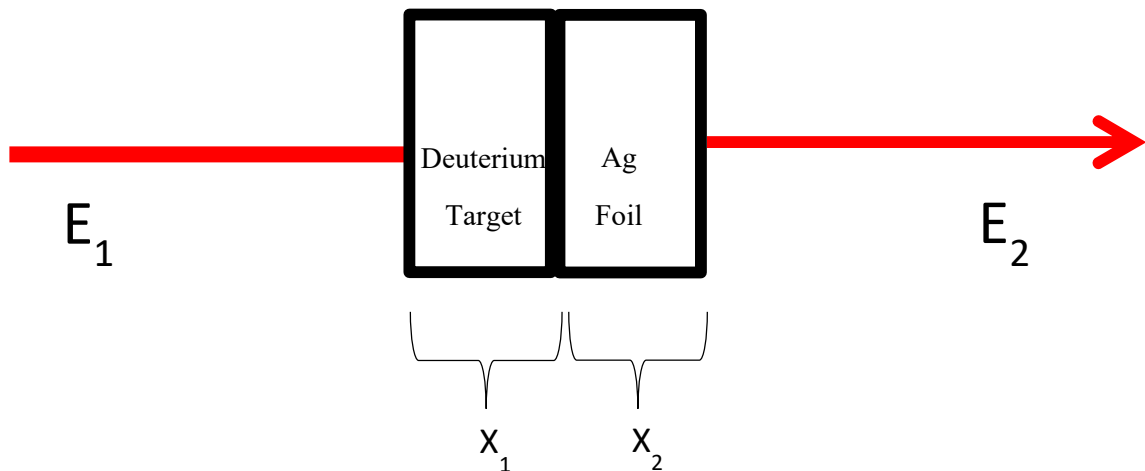

Figure 3.3: Diagram showing schematically the variables involved in the calculation of energy loss.
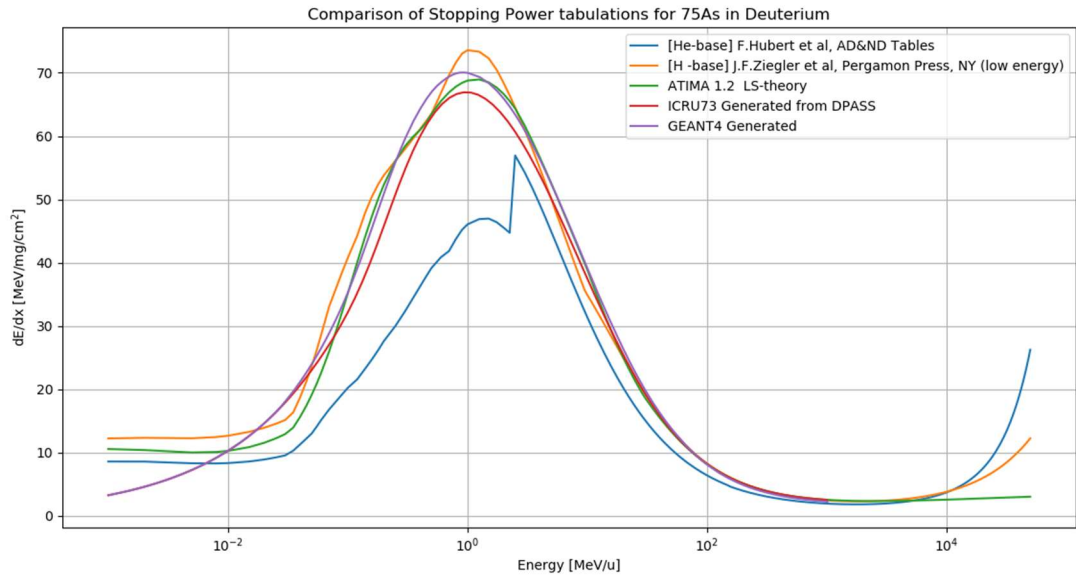
Figure 3.4: Comparison of tabulated values of ^{75}As energy loss in deuterium.
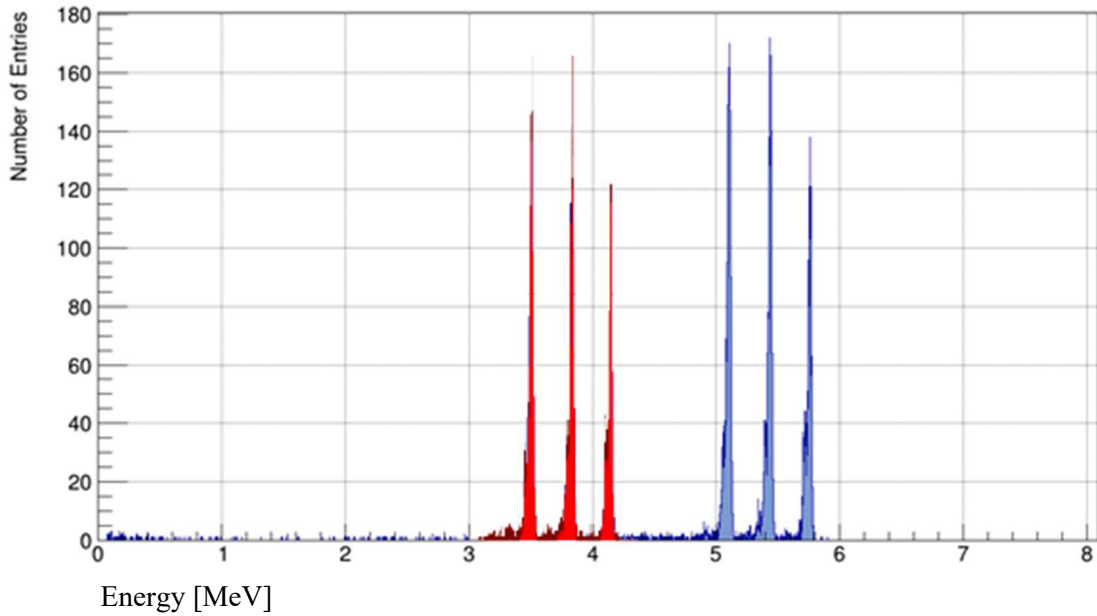

Figure 3.5: Plot showing energy spectra of triple alpha source between foil and detector (blue) and behind foil (red), displaying the observable shift in energy.

3.5 Downstream S3 Calibration and Deuterium Target Thickness Measurement

With the thickness of the silver foil now a known parameter, the downstream S3 detector may be calibrated, and applying this calibration, the thickness of the deuterium target may then be measured. The process for calibrating the S3 detector is similar to that employed to calibrate the YY1. As discussed, the downstream S3 detector is responsible for observing heavy, beam like nuclei, which are orders of magnitude more energetic than the alpha source, necessitating the use of the beam itself in calibration of the downstream S3, in order to avoid any non-linearity in the detector gain, as previously mentioned.

Evidently, it is necessary to understand the thickness of the silver foil, as while the energy of the emitted alpha particles used in the calibration of the upstream detectors was known, to understand the energy deposited by a beam constituent on the S3 detector, the energy of the beam as it enters the IRIS apparatus must be known, the energy lost by the particle as it passes through the IC, the energy lost as it scatters through the silver foil, as well as the energy lost by the particle as it travels through the detector dead layer, a thin inactive material layer on either side of the active silicon layer, must all be calculated.

This process is applied to data taken before the deuterium target is formed, so it need not be considered. Calculating these energy losses for the various ^{50}Ca beam constituents, ^{25}Mg, ^{50}Ti, ^{50}Cr and ^{75}As, fitting the observed spectra with gaussians and using their means to determine ADC channel number, the gain may be calculated as the mean of that calculated by each species individually. Finally, pedestals may be determined by the process outlined in Section 3.3.

In measuring the thickness of the deuterium target, a method similar to that applied in measuring the silver foil thickness is used. The primary difference being, the beam and now calibrated S3 detector are employed in place of the alpha source. The other difference being that the deuterium target has two thicknesses to be measured, the first is approximately 50 µm, formed near the beginning of the experiment, after collecting foil-only data, and the second is approximately 100 µm, as additional deuterium was added to the target mid-way through the course of the experiment. Using spectra taken before and after target formation, and once again observing the shift in incident particle energy for the beam species, the width of the target may be measured by applying tables of energy loss through deuterium by the particles of interest, such as the one shown in Fig. 3.5. The result of this process is shown in Fig. 3.6.
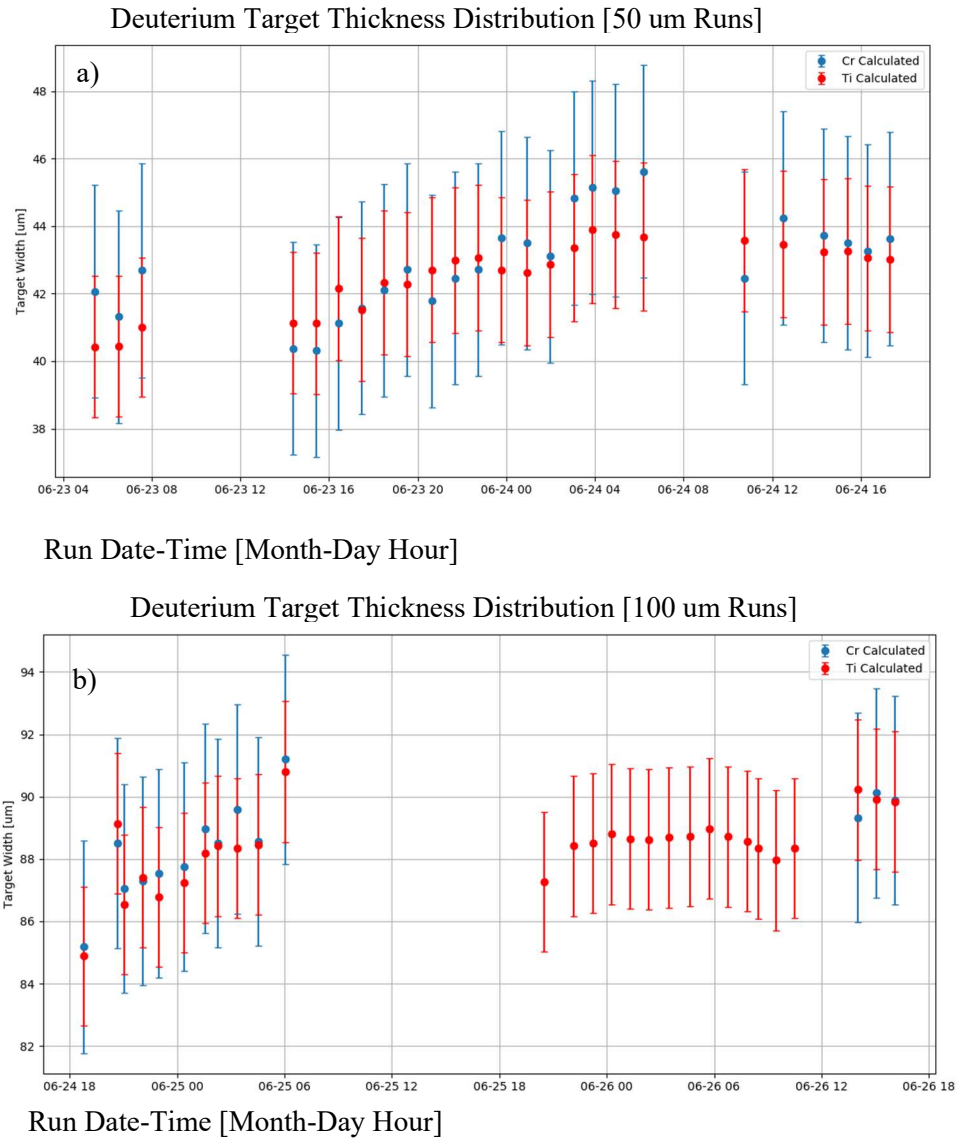
Deuterium Target Thickness Distribution [50 um Runs]

Run Date-Time [Month-Day Hour]

Deuterium Target Thickness Distribution [100 um Runs]

Run Date-Time [Month-Day Hour]

Figure 3.6: By-Run target thickness calculations for ~50 µm and ~100 µm experiment runs using ^{50}Cr and ^{50}Ti.

In Fig 3.6, apparent increases in the measured target thickness for both thin and thick target runs are clearly visible. This is a puzzling result, as if any change at all would be to occur, it would be expected that the target thickness would shrink over time due to potential radiative heating. The explanation for this comes by investigating the IC spectrum. As has been discussed, the method of target thickness measurement relies only on the energy lost by the beam through the IC, deuterium target, silver foil and detector dead layer. If the energy lost in any of these materials were to be greater in reality than what was calculated, the additional energy loss would be attributed to the thickness of the target in the calculation.

The IC was the source of this discrepancy. Fig. 3.7 a) plots the average temperature of the Ionization Chamber over the course of the experiment on a bi-hourly basis, in which clear oscillations may be seen. As the pressure and volume of the gas filled chamber are controlled and fixed, an increase in the temperature leads to a decrease in the number of isobutane molecules present in the chamber, and vice versa, as is related by the ideal gas equation of state.

$$P \times V = n \times R \times T \qquad (3.3)$$

With P being pressure, V being volume, n corresponding to the number of moles of the gas, R being the ideal gas constant and T, the temperature of

the gas. An increase in the number of isobutane molecules would then lead to an increase in "thickness" as seen by any incident particle, and an increase in its energy lost through the gas volume.
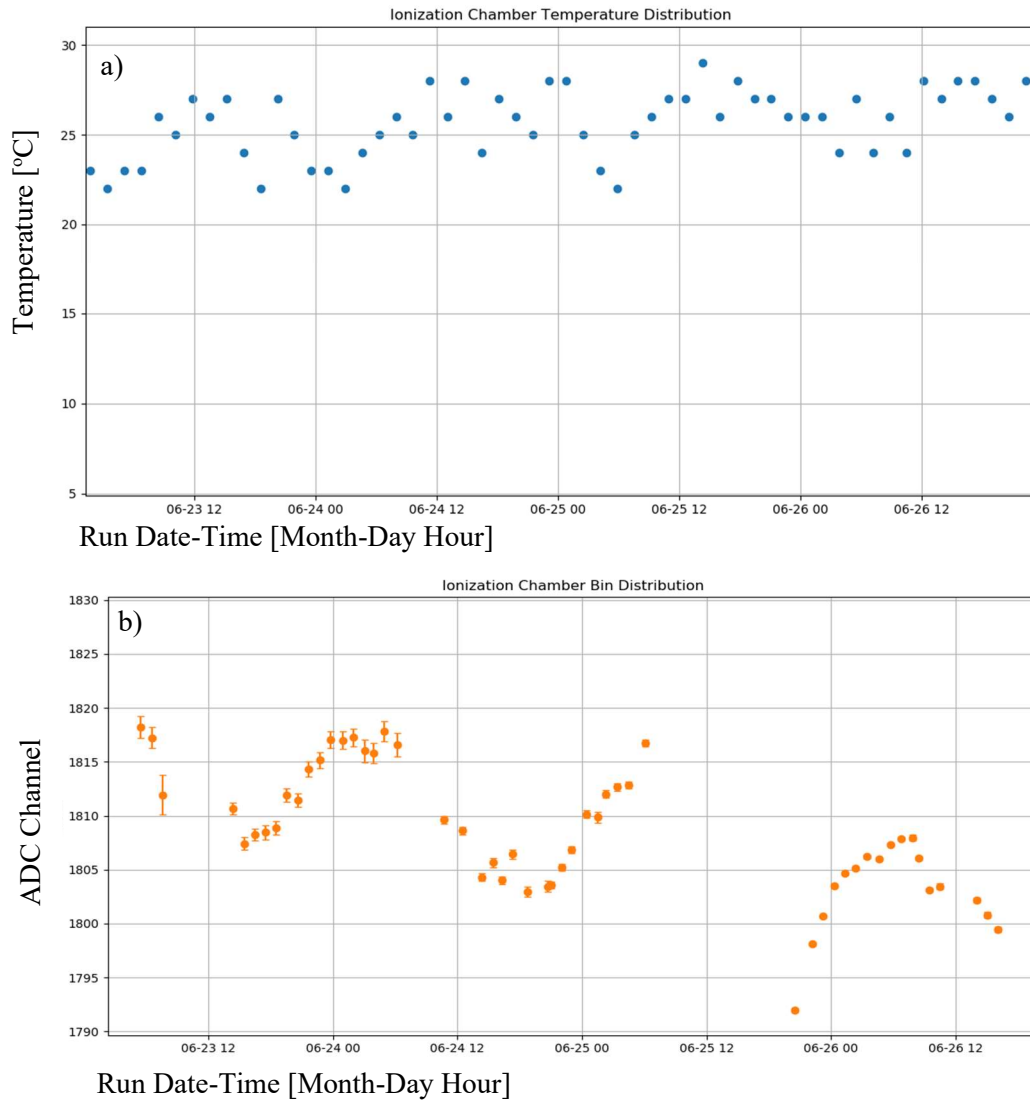

Figure 3.7: a) Plot of bi-hourly IC temperature averages over the course of the experiment. b) Plot of ^{75}As IC ADC Channel for each experimental run.

As can be seen in Fig. 3.7, the temperature oscillations of the Ionization Chamber and the oscillations in the energy deposited by ^{75}As in it have a similar period. The apparent increases in target thicknesses seen in Fig. 3.7 can be seen to happen on similar timescales as well, such as the time period from 06-23 12 to 06-24 06, suggesting a correlation between the two phenomena.

This was taken into account as an additional source of uncertainty in the target thickness measurement, proportional to the measured target thickness if the IC temperature had been at it's extremum. This was added to the inherent uncertainty consisting of the error in the means of the fitted gaussians in the detector spectra, and an added 2% error accounting for variations in energy loss tables. The measured target thicknesses were then fit using a least-squares method to find the single best value for both the ~ 50 μm group of runs and the ~ 100 μm group of runs. This resulted in measured target thicknesses of 43 ± 2 μm and 89 ± 3 μm.

3.6 Downstream YY1 and CsI (TI) Calibration

The combination of the downstream YY1 and CsI (TI) detectors observe the angle and energy of deposited light particles, such as protons, deuterons tritons and alpha particles. Here the fundamental process of detector calibration is once again repeated. While the downstream YY1 was calibrated using a triple alpha source as discussed in section 3.3, the incident particles used in calibration for the CsI (TI) detector were deuterons produced in the $^{40}Ar(d,d)^{40}Ar$ scattering reaction, ^{40}Ar being a stable beam sent to IRIS prior to the delivery of the radioactive ^{50}Ca beam, applied for its higher count rate. These deuterons may be distinguished from the protons, tritons and alpha particles also present in these detector spectra by applying the understanding that each of these light particles has a maximum amount of kinetic energy it may deposit in the YY1, due to the energy deposited in a material being inversely proportional to kinetic energy. Thus, a particle with more energy than the maximum will depart less on its way through the YY1, and the remainder in the CsI (TI) as it comes to rest. This is illustrated in Fig. 3.8, with a particle identification spectrum.

With the deuterons identified, the energy they would deposit in the detector must then be calculated. Once again, this involves calculating the

energy lost by the ^{40}Ar as it travels through the IC windows and active gas volume, and then the resultant energies of the scattered deuteron and ^{40}Ar after their interaction. As this interaction happens at a random point in the deuterium target, for the purposes of calculation it is approximated to be the middle. The energy lost by ^{40}Ar through the first half of the target must therefore also be calculated. The energies of the resultant particles after the scattering reaction are dependent upon the angle at which they are ejected, and this must be taken into account as the energies lost by the deuteron in the second half of the deuterium target, silver foil, YY1 dead and active layers as well as the CsI (TI) dead layer are all calculated.

With the final deposited energy in the CsI (TI) evidently being dependent upon the incident angle of the particle, it is necessary to resolve this angle in the CsI (TI) spectra. This is done by gating on events in the spectra that correlate to events in particular chosen angular segments of the YY1, creating a virtual angular segmentation in the CsI (TI). Due to low count rates, instead of gating on each of the 16 individual YY1 angular segments in the CsI (TI) spectra, the calibration was carried out in groups of four angular segments.
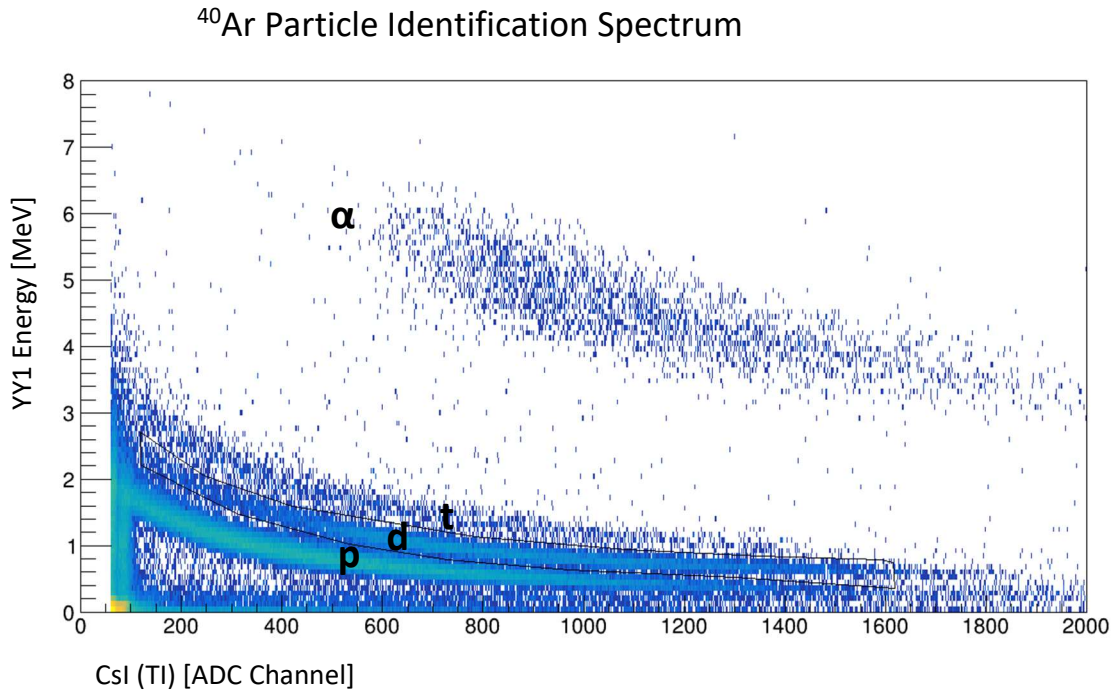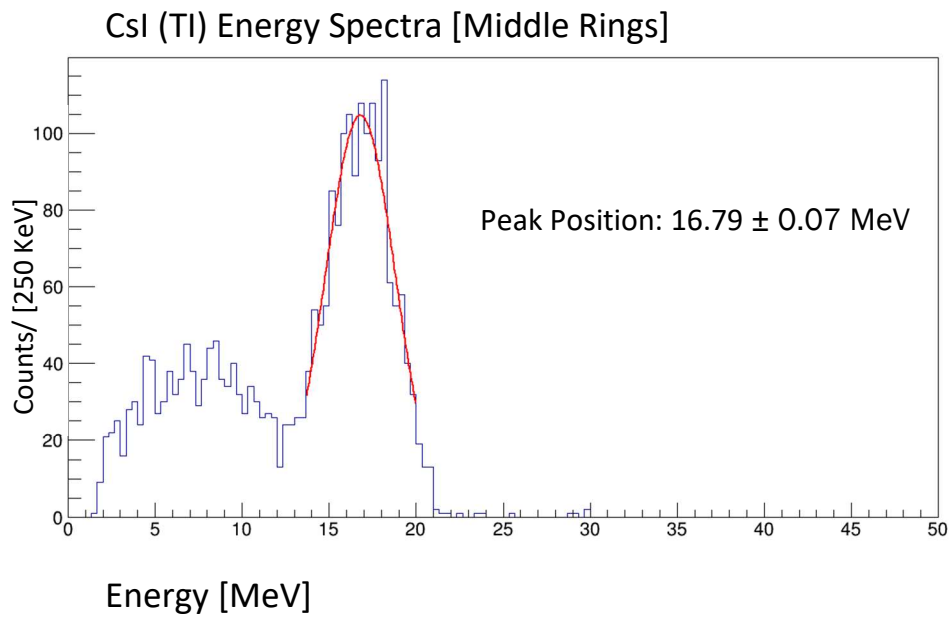
^{40}Ar Particle Identification Spectrum

Fig. 3.8: Plot of 2D particle identification spectrum, with visible proton, deuteron, triton and α particle bands.

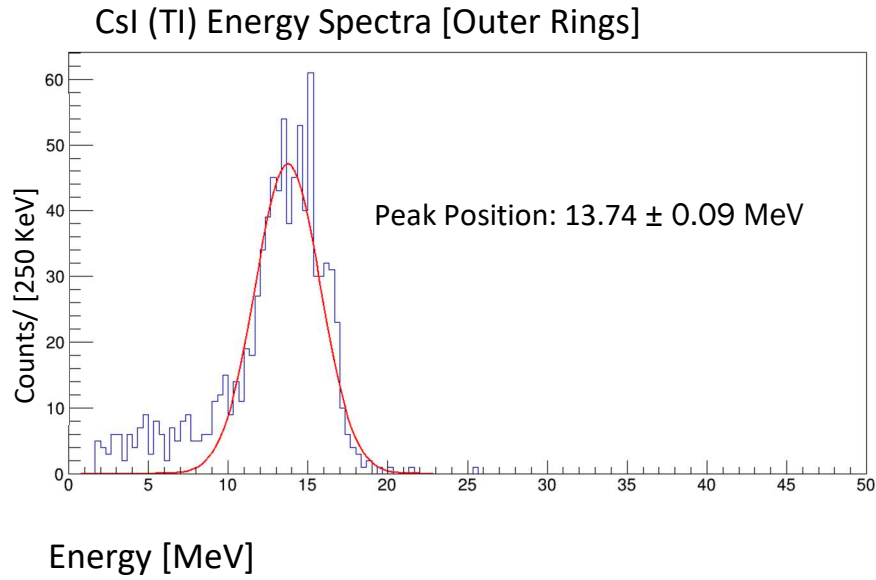## CsI (TI) Energy Spectra [Middle Rings]

Peak Position: 16.79 ± 0.07 MeV

Fig. 3.9: ^{40}Ar CsI (TI) 1D energy Spectrum illustrating angular dependance
of deposited energy.

3.7 Derivation of ^{50}Ca(d,d)^{50}Ca Q-Value Spectra

The Q-Value of a nuclear reaction is defined as the following.

$$Q = m_A + m_b - m_C - m_d \qquad (3.4)$$

The sum of the masses of the incoming particles minus that of the outgoing particles. In a scattering interaction such as the reaction of interest,

^{50}Ca(d,d)^{50}Ca, there is the possibility of inelastic scattering, wherein the outgoing ^{50}Ca would enter an excited state, and the corresponding m$_C$ would be unknown. The expression may then be re-written in the following manner.

$$Q = m_A + m_b - m_d - \sqrt{E_C^2 - P_C^2} \qquad (3.5)$$

In which E$_C$ and P$_C$, the energy and momentum of the resultant beam like particle, are defined in terms of the following experimentally observed and known quantities.

$$E_C = E_{Beam} + m_A + m_b - E_d - m_d \qquad (3.6)$$

$$P_C = \sqrt{P_A^2 + P_d^2 - 2P_A P_d \cos\theta_d} \qquad (3.7)$$

With E$_{Beam}$, m$_A$, m$_b$, m$_d$, P$_A$ being known quantities, and the remaining quantities being measured by IRIS. In the case of inelastic scattering, a non-zero Q-Value would then correspond to the excited states of the reaction in the following manner.

$$E_{excited} = Q - Q_{gs} \qquad (3.8)$$

With the experimental information collected, the Q-Value may then be constructed for each interaction, giving insight into the excited states of the nucleus, and acting as a step towards information regarding nuclear structure.

The Q-Value spectra resulting from this experiment are shown in Fig. 3.10, with the spectrum corresponding to the thicker deuterium target being subdivided into angular regions. In both sets of data, a peak is visible at 0, or the ground state of ^{50}Ca. In both cases, it is also difficult to attempt to resolve any further excited states. It is also of note that the ground state peak of each spectrum was fit with a gaussian and compared to the fit of a simulated ground state gaussian, of which the gaussian fit to simulation had a standard deviation smaller by an approximate factor of two. More precisely, the standard deviations of the thick target spectra are $\sigma_{data} = 0.87 \pm 0.1$ and $\sigma_{simulated} = 0.534 \pm 0.005$. The thin target spectra have standard deviations of $\sigma_{data} = 0.78 \pm 0.3$ and $\sigma_{simulated} = 0.368 \pm 0.005$. This is possibly due to error arising in the calibration of the CsI (TI) as a result of low count rates in a number of angular regions, a result of the low number of statistics in the Q-Value spectra, or a result of a possible nearby unresolved excited state. However, a sum of two gaussians was also fit to the peak and compared appropriately to simulation, the result being a still wider ground state gaussian.
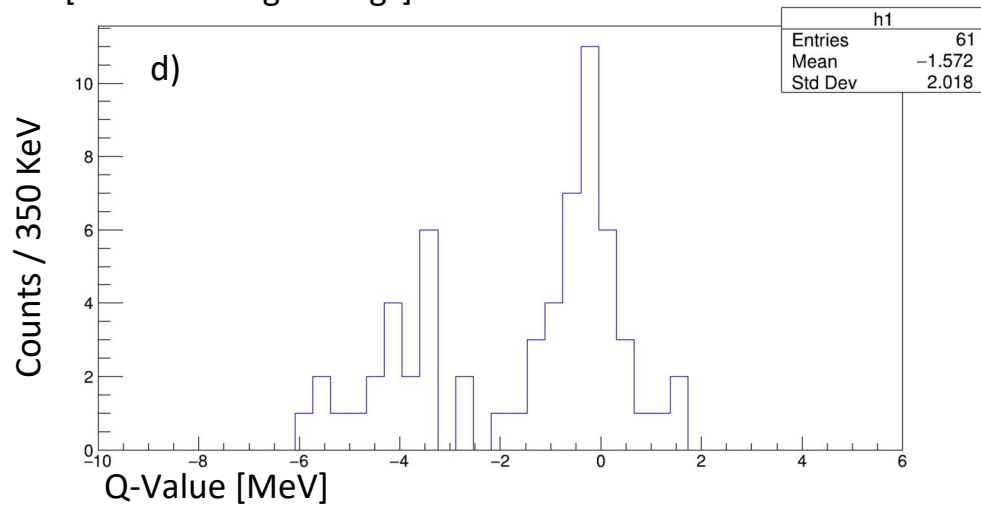
Thin Target ^{50}Ca(d,d)^{50}Ca Q-Value Spectrum

Thick Target ^{50}Ca(d,d)^{50}Ca Q-Value Spectrum
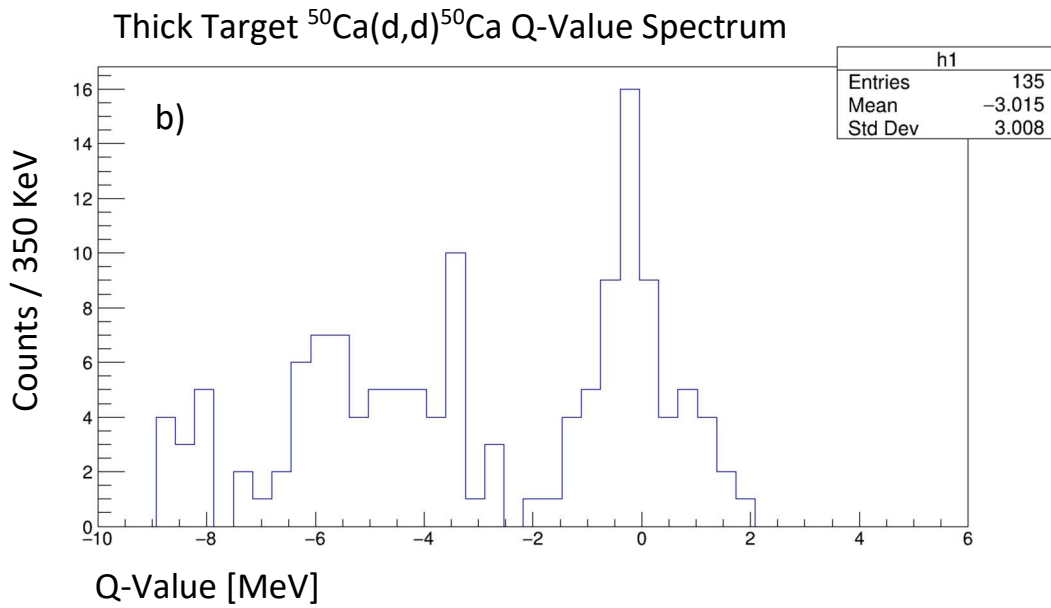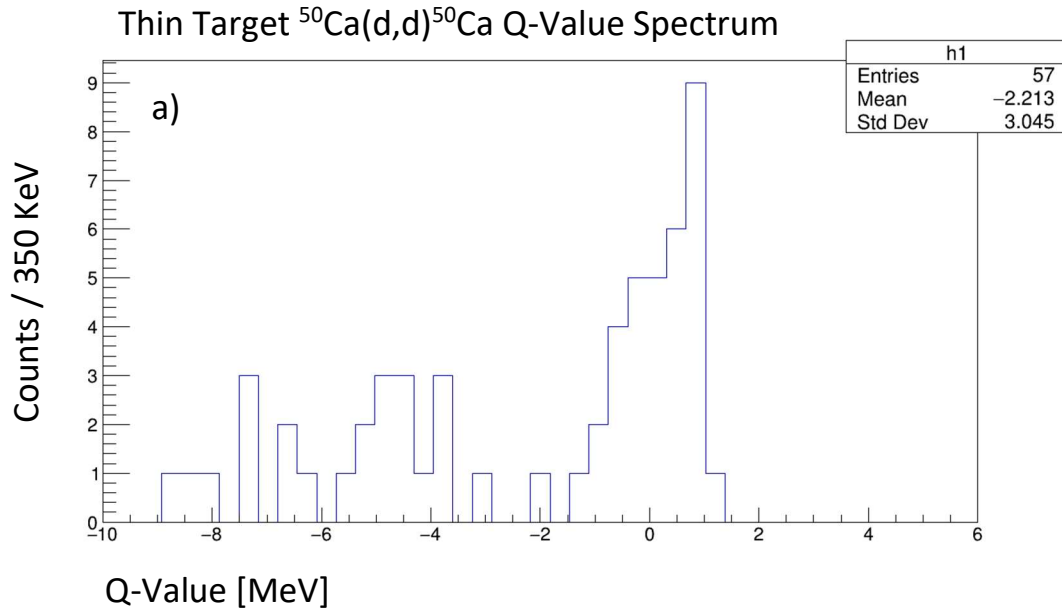
Thick Target ^{50}Ca(d,d)^{50}Ca Q-Value Spectrum

[YY1 Inner Eight Rings]
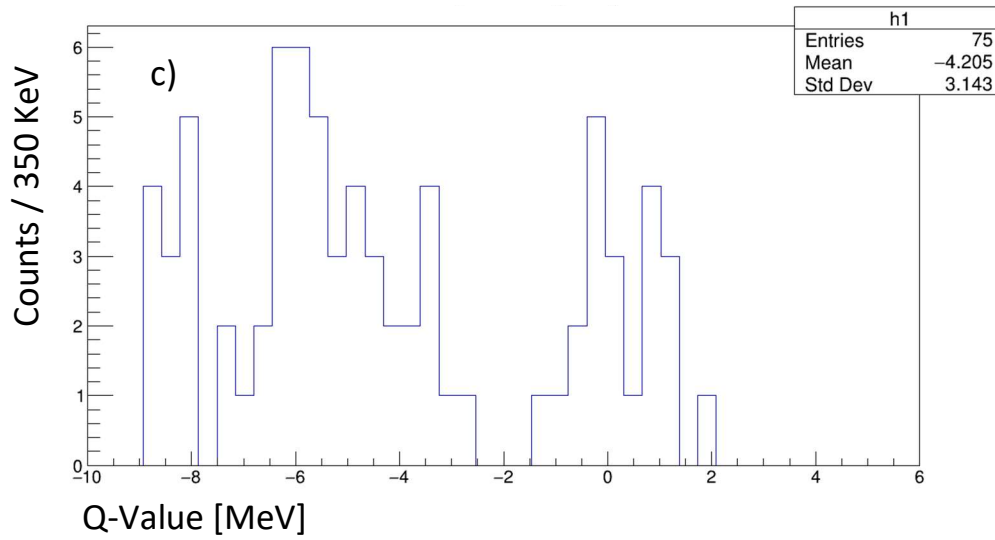
Thick Target ^{50}Ca(d,d)^{50}Ca Q-Value Spectrum

[YY1 Outer Eight Rings]

Fig. 3.10: Measured Q-Value spectra for the ^{50}Ca(d,d)^{50}Ca reaction

Chapter 4
Discussion

The current experimental understanding of the excited states of ^{50}Ca and their properties is limited, with the majority of the spin and parity (J^{π}) assignments of states above the first 2^{+} excited state at 1.026 MeV remaining tentative, if they are known at all. There are two points of particular interest in the observed data. The first is the lack of visibly populated excited states between 1 and 4 MeV. While the previously mentioned first excited state may be unresolvable due to its proximity to the ground state peak, the absence of the other four other states quoted in this region may be an artifact of the low number of counts. The second point of interest is the structure visible near -5.5 MeV in the thick target spectra. There are a large number of closely spaced states cited in literature within this region (i.e., 10 reported states exist between -5.5 MeV and -5 MeV). This may possibly be the source of the structure, if only a number of these states are populated with only a low number of counts, the density of states alone may give rise to the observed structure. Figure 3.12 shows a single gaussian with a fixed peak fit of -5.576 MeV fitted within the bounds -4.08 MeV to -7.08 MeV for both the thick target data and a simulated peak of the same energy, which takes into account

only experimental resolution. The width of the gaussian fitted to the data is approximately a factor of three wider than that of the simulation ($\sigma_{data} = 0.89$, $\sigma_{simulation} = 0.28$), this may be due to the contribution of the numerous nearby states. Beyond the state at 1.026 MeV, no excited states have spin assignments, which this project may help to elucidate. However, the low number of counts would be a significant obstacle in this endeavor. The first 24 known excited states for ^{50}Ca are collated in table 5.1. The calibrations obtained for this project may also aid in the analysis of the ^{50}Ca(d,p)^{51}Ca reaction.
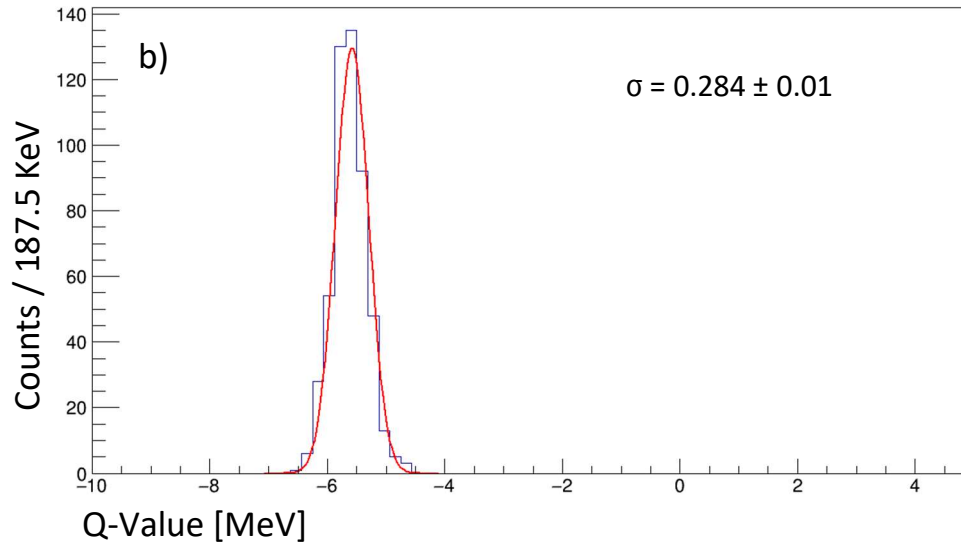
Thick Target ^{50}Ca(d,d)^{50}Ca Q-Value Spectrum
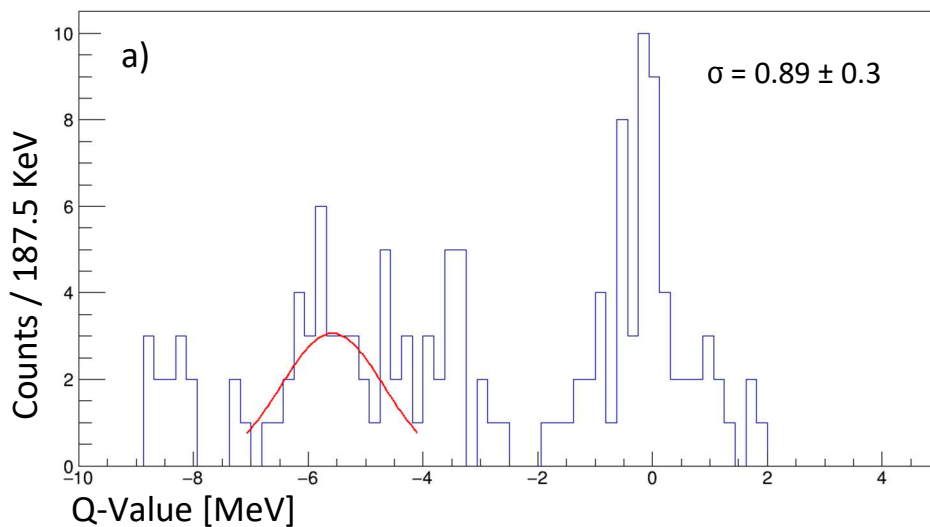
Simulated ^{50}Ca(d,d)^{50}Ca -5.576 Q-Value Peak

Fig 3.12: Gaussian fit with fixed peak of -5.576 MeV for both thick target

spectra and simulated Q-Value gaussian peak of the same energy.

Excited State Energies [MeV]

1.026	4.830	5.147
3.002	4.870	4.168
3.531	4.886	5.281
3.997	4.970	5.362
4.035	5.043	5.424
4.475	5.084	5.516
4.515	5.109	5.576

Table 5.1: Energies of the first 21 known excited states of ^{50}Ca

References

[1] Otsuka, T. et al. (2020). Evolution of shell structure in exotic nuclei. *Reviews of modern physics, 92*, 1-52

[2] Mayer, M.G. (1949). On Closed Shells in Nuclei II. *Physical Review, 75,* 1969-1970

[3] Haxel, O., J.H.D. Jensen, H.E. Suess (1949). On The "Magic Numbers" in Nuclear Structure. *Physical Review, 75,* 1766

[4] Huck, A. et al. (1985). Beta decay of the new isotopes ^{52}K, ^{52}Ca, and ^{52}Sc; a test of the shell model far from stability. *Physical Review C, 31*, 2226-2237.

[5] Dinca, D.-C. et. al. (2005). Reduced transition probabilities to the first 2+ state in Ti52,54,56 and development of shell closures at N=32,34. *Physical Review C, 71.*

[6] R. Chapman, S. Hinds, A.E. Macgregor, (1968). A Study of ^{52}Cr, ^{54}Cr and ^{56}Cr by the (t, p) Reaction. *Nucl. Phys. A.,* 305.

[7] Prisciandaro, J.I. et al. (2001). New evidence for a subshell gap at N = 32. *Physics Letters B, 510,* 17-23.

[8] Ostuka, T. et. al. (2001). Magic numbers in exotic nuclei and spin-isospin properties of the NN interaction. *Phys. Rev. Lett., 87.*

[9] Rejmund, M. et. al. (2007). Shell evolution and the N = 34 'magic number'. *Physical Review C, 76*, 1-5.

[10] Steppenbeck, D. et. al. (2013). Evidence for a new nuclear 'magic number' from the level structure of ^{54}Ca. *Nature, 502*, 207-210.

[11] Gallant, A. T. et. al. (2012). New precision mass measurements of neutron-rich calcium and potassium isotopes and three nucleon forces. *Phys. Rev. Lett., 109*.

[12] Wienholtz, F. et. al. (2013). Masses of exotic calcium isotopes pin down nuclear forces. *Nature, 498*, 346-349.

[14] Michimasa S. et. al. (2018). Magic nature of neutrons in ^{54}Ca: First mass measurements of $^{55\text{-}57}$Ca. *Phys. Rev. Lett., 121*.